Plasma-enhanced detonability: experimental and calculated reduction of the detonation cell size

Mhedine Ali Cherif, Ryu Masuda, Alain Claverie, Pierre Vidal, Svetlana Starikovskaia

Full-length paper, 25 November 2024

Plasma-enhanced detonability: experimental and calculated reduction of the detonation cell size

Mhedine Ali Cherif[1]‡, Ryu Masuda[1]§, Alain Claverie[2], Svetlana M. Starikovskaia[1]‖, Pierre Vidal[2]

[1] Laboratoire de Physique des Plasmas, UMR 7648 CNRS, Ecole Polytechnique, 91128 Palaiseau, France

[2] Institut Pprime, UPR 3346 CNRS, ENSMA, 86034 Chasseneuil-du-Poitou, France

Abstract. This work analyzes the interaction between non-equilibrium plasma and detonation. The aim is to enhance the detonability of gaseous mixtures by reducing the detonation cell width through dissociation of a fresh gas mixture by plasma action. The experiments were performed in a square-section detonation tube, and the diagnostic tools used were ICCD chemiluminescence imaging, soot-plate recording, dynamic pressure sensors, and back current shunt technique. The results show that the application of a nanosecond plasma ahead of a self-sustained detonation reduces the cell width by a factor of about 2 in H_2:O_2:Ar, H_2:O_2, CH_4:H_2:O_2:Ar and CH_4:O_2:Ar mixtures for initial pressures between 100 and 200 mbar. A parametric study of plasma properties focused on the effect of the initial pressure on the deposited energy and homogeneity. A kinetic mechanism was proposed to estimate the dissociation effect of plasma chemistry on the fresh combustible mixture. The obtained densities of atoms produced in the plasma were used as input parameters to calculate the thermicity and temperature profiles of the detonation reaction zone according to the Zel'dovich-von Neumann-Döring model. The reduction factor of the ZND characteristic chemical length is about the same as the experimental cell widths, i.e. 2. This combination of experiments and calculations substantiates the relationship between plasma parameters, ZND chemical lengths, and detonation cell widths and, thus, demonstrates the possibility of controlling detonability using a nanosecond discharge.

‡ Present address: Clean Combustion Research Center (CCRC), King Abdullah University of Science and Technology, Thuwal 23955-6900, Saudi Arabia

§ Present address: Department of Mechanical Engineering, School of Engineering, Tokyo Institute of Technology, Yokohama, 226-8502, Japan

‖ Corresponding author: svetlana.starikovskaia@lpp.polytechnique.fr

Novelty and significance

The novelty is the first experimental demonstration that the action of a non-equilibrium plasma on a fresh combustible mixture can instantaneously produce enough atomic species ahead of a self-sustained detonation front to reduce by about half the mean width of the cells that structure the detonation reaction zone in gases. The significance is that a nanosecond discharge is now proven to be a means of controlling detonability, here considered as the ability of a detonation to propagate in a device of given transverse dimensions, since the smaller the cells, the higher the detonability.

Author contributions

MAC: performed research, analysed data, wrote the paper
RM: analysed data
AC: synchronized the plasma and detonation triggering and vizualisations
SMS: designed the experiments, analysed data, reviewed and edited the paper
PV: designed the experiments, analysed data, reviewed and edited the paper

Keywords

Nanosecond discharge, plasma, detonation, cellular structure, detonability

Declaration of interests

The authors declare that they have no known competing financial interests or personal relationships that could have appeared to influence the work reported in this paper.

1. Introduction

The study and understanding of the detonation phenomenon is of great practical and fundamental interest. Reliable control of detonation mitigation, initiation or propagation is essential for applications such as pressure gain devices, which include industrial safety [1, 2] and pressure gain power generation [3, 4] and propulsion [5–7], for example pulsed or rotating detonation engines (PDEs, RDEs) [7]. Thus, given a confinement, detonability can refer to the ability of a detonation to propagate steadily as close as possible to the ideal regime or the ability of a deflagration to transition to detonation as close as possible to ignition: the smaller the transverse dimension of the confinement for self-sustained detonation propagation or the shorter the distance to self-sustainment, the higher the detonability of the mixture considered. Multidimensional detonations in gases have a cellular structure, i.e. a grouping of Mach waves consisting of forward propagating convex shocks bounded by shocks propagating transversely with respect to the main direction of propagation of the detonation, e.g. [8]. The elements of this structure are commonly referred to as detonation cells. With regard to detonation propagation in a device of a given transverse dimension, the more cells there are on the detonation front, the easier the propagation. This work shows that applying plasma generated by nanosecond discharges ahead of a detonation front can improve detonability by instantaneously increasing the number of cells on the front.

Combustion ignition occurs in the domains behind the transverse fronts and the fastest forward propagating fronts of the cellular structure. The process then continues adiabatically or with some participation of turbulent diffusion, mostly determined by chemical kinetics. Many experimental, numerical and theoretical analyses of the detonation cell structure have been available for decades. Most of the recent contributions, e.g. [9–16], incorporate and discuss older works. Understanding the cellular structure is necessary for many applications because the cell mean width λ can be a characteristic length useful in determining the detonability of a mixture. For detonation propagation in a channel, a criterion is obtained from comparing λ with the transverse dimension L of the channel , i.e. the smaller λ/L, the higher the detonability. However, this requires the mean width λ to be statistically significant. The number of cells analyzed on the same longitudinal recording should be large enough, and the dispersion of their measured widths low enough, i.e. the standard deviation relative to the mean width should be low. In any case, the mean width should be one order of magnitude smaller than the smaller transverse dimension of the channel [17]. These conditions are met in large channels with mixtures for which the cellular combustion process is adiabatic, i.e. for which the cells are not too highly irregular.

From the phenomenological point of view, the self-sustained detonation regime in channels is referred to as multi-cellular when the number of cells on the front surface is large enough, typically $\mathcal{O}(100)$, i.e. $\mathcal{O}(10)$ in the smaller transverse dimension of the

channel. In this case, the cellular dynamics, and therefore the cell mean width, can be assumed to depend only on the combustion process. Otherwise, the cell dynamics also depends on the transverse dimension, and the detonation regime is referred to as marginal. The cell mean width increases with decreasing initial pressure and is all the greater when the stoichiometry is unbalanced. Its dependence on initial temperature may be non-monotonic depending on the mixture composition and the constraint imposed on the temperature variation, e.g. constant initial pressure or volume.

Three-dimensional numerical simulations, e.g. [13], appear to be the only realistic approach today to model the dynamical behaviours of cellular detonations. However, large computational resources remain necessary to represent a large enough number of cells and combine detailed mechanisms of chemical and physical kinetics and transfer phenomena. Examples include non-thermal equilibrium effects, e.g. [18–21], carbon condensation in rich carbon mixtures, e.g. [22], and turbulent diffusion involved in deflagrative subdomains such as those observed in reaction zones with highly irregular cells, e.g. [23–25]. A cell mean width λ is often accepted to be proportional to a characteristic length of the planar detonation reaction zone in the Zel'dovich-Von Neuman-Döring (ZND) model [26], and correlations are available, e.g. [27], which combine properties of ZND profiles and experimental data. The ZND length is the sum of the thicknesses of the induction and main reaction layers, but is often approximated by the position of the thermicity maximum relative to the shock. Thermicity is proportional to the rate at which chemical changes contribute to hydrodynamics compared to isentropic evolutions [28]. For an ideal gas, its ZND profile will have a maximum located approximately at the same distance from the shock as the inflection point of the temperature profile, e.g. [26, 27]. A difficulty is that many measurements are made in confinements whose transverse dimensions are too small and, therefore, influence the cell dynamics and widths, while the planar ZND model refers to detonation independent of the confinement. A model for predicting mean widths on detonation fronts with a large number of cells has recently been proposed but requires a chemical kinetic mechanism validated for the thermodynamic range of the detonation reaction zone and the chemical composition of the mixture. [16, 17].

Therefore, the usefulness of the cell mean width for characterizing the cell structure should not be overestimated, as the regularity and the number of cells should be large enough for a mean width to be statistically significant. In applied situations, this may be difficult to achieve due to the technological constraints imposed by the configuration and the dimensions of the device and the initial composition, pressure and temperature of the mixture. Thus, a practical approach to enhancing detonability, given the dimensions of the device, is simply to increase the number of cells by increasing the initial pressure or by modifying the initial chemical composition of the mixture, regardless of cell regularity and whether or not a statistically significant mean width exists or can be calculated.

For example, Crane et al. [29] experimentally observed a significant reduction in cell width, up to 70%, by introducing a small amount of ozone (3000 ppm) into H_2:O_2 mixtures diluted with either Ar or N_2 (50%) and the equivalence ratio ranging from 0.4 to 1.5. Indeed, the induction lengths were reduced with little change in the main reaction thicknesses and Chapman-Jouguet (CJ) velocities. The ozone addition was achieved by pre-mixing, which imposes time and technological constraints.

Another possibility for locally enhancing chemical reactivity is the direct generation of atoms and radicals by non-equilibrium plasmas. Recent reviews discuss energy branching as a function of electron energy in combustible mixtures and changes in the efficient activation energy [30, 31]. Pulsed nanosecond discharges, allowing high electric fields, provide efficient dissociation [32] faster than the typical combustion characteristic times. In the field of plasma-assisted combustion, experimental and numerical studies have demonstrated a reduction in ignition delay [32], an extension of flammability limits and improved combustion stability in lean mixtures [31, 33]. Shock tube experiments have shown a significant reduction in ignition delay (by 3-4 orders of magnitude) for methane-based mixtures [34] due to dissociation occurring during discharge and partial reforming of the mixture in the near afterglow.

Enhancement of the deflagration-to-detonation (DDT) transition [35] by non-equilibrium plasma has been investigated in several experimental and numerical studies [36–38]. They show that the combination of thermal, chemical and hydrodynamic effects can significantly reduce the characteristic time and distance of the DDT process. In contrast, research into the influence of plasma on an established detonation and its parameters is limited and mainly numerical [39]. Nevertheless, recent experiments in a rotating detonation combustor show that applying a nanosecond high voltage discharge allows the existence of detonation outside standard operating conditions, with a strong dependence on the discharge geometry [40]. Another experimental study in a channel demonstrates the instantaneous cell size reduction by applying nanosecond discharges to the fresh gas just before the cellular detonation front [41].

The present experimental and numerical work extends the previous study [41]. First, the reduction of the detonation cell size under the action of a non-equilibrium plasma is obtained experimentally for several gas mixtures and initial pressures. Then, a model of plasma kinetics for the dissociation of the fresh gas and ZND calculations of the detonation reaction zone with detailed chemical kinetic mechanisms are combined to analyse the detonation cell properties with and without plasma. Finally, a comparison of the experimental and numerical results establishes a clear correlation between the reduction of the detonation cell size and the dissociation of the fresh gas by nanosecond discharge.

2. Experimental setup and methodology

The experiments aimed to obtain information on whether and how a high-voltage (HV) nanosecond discharge produces homogeneous plasma in the fresh gas, just before the detonation front, and if this plasma modifies the detonation cellular structure.

Figure 1 shows a schematic of the setup, which consisted of two parts, (1) the detonation tube, where the detonation was initiated and reached the Chapman-Jouguet regime, and (2) the diagnostic chamber, which continued the tube and where the nanosecond discharge was generated in front of the detonation front after it enters the chamber. The tube and the chamber had the same 50x50 mm^2 square cross-section and were made of stainless steel. Apart from the elements necessary to control the discharge, the setup was the same as that developed to study detonation propagation, quenching and reinitiation in stratified gas mixtures [42, 43].

The devices for the detonation velocity measurement and the cell pattern recording were mounted on the same wall of the diagnostic chamber, opposite to the high-voltage electrode. A typical experiment consisted of two steps as these devices were different.

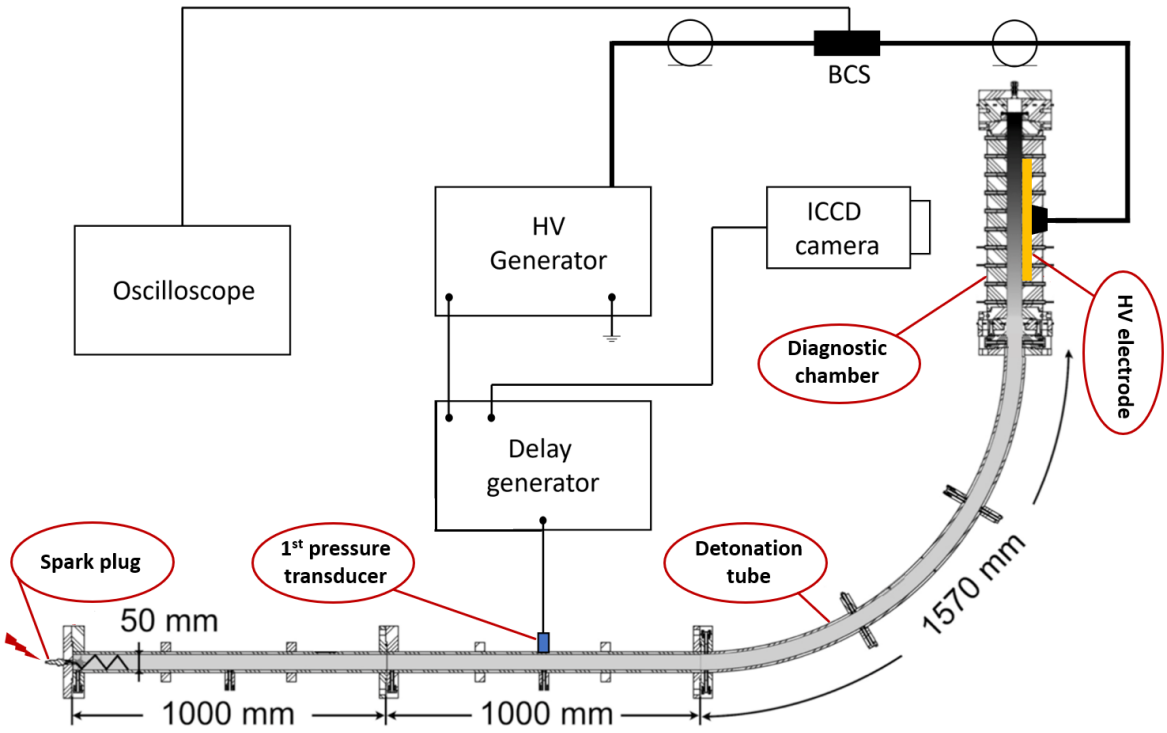

Figure 1: Schematic of the experimental setup showing the detonation tube in grey with the ignition spark plug at its left end and the diagnostic chamber at its top right, the HV electrode in yellow at the right side of the chamber, and the 1^{st} pressure transducer, which triggers the synchronization sequence when detecting the detonation wave.

The first one was the velocity measurement, and the second one was the cell pattern recording, without and with the plasma discharge. Information on the velocity was obtained using the signals from piezoelectric pressure transducers triggered by the detonation (ten Kistler 603B transducers, response time 1 μs, natural frequency 300 kHz) connected to Kistler 5018A electrostatic charge amplifiers (bandwidth 200 kHz)]. Information on cell patterns was obtained using the classic technique of recording on carbon deposition (soot) plates, here implemented with stainless steel plates (1 mm thick, 50×650 mm^2), which also acted as the grounded electrode.

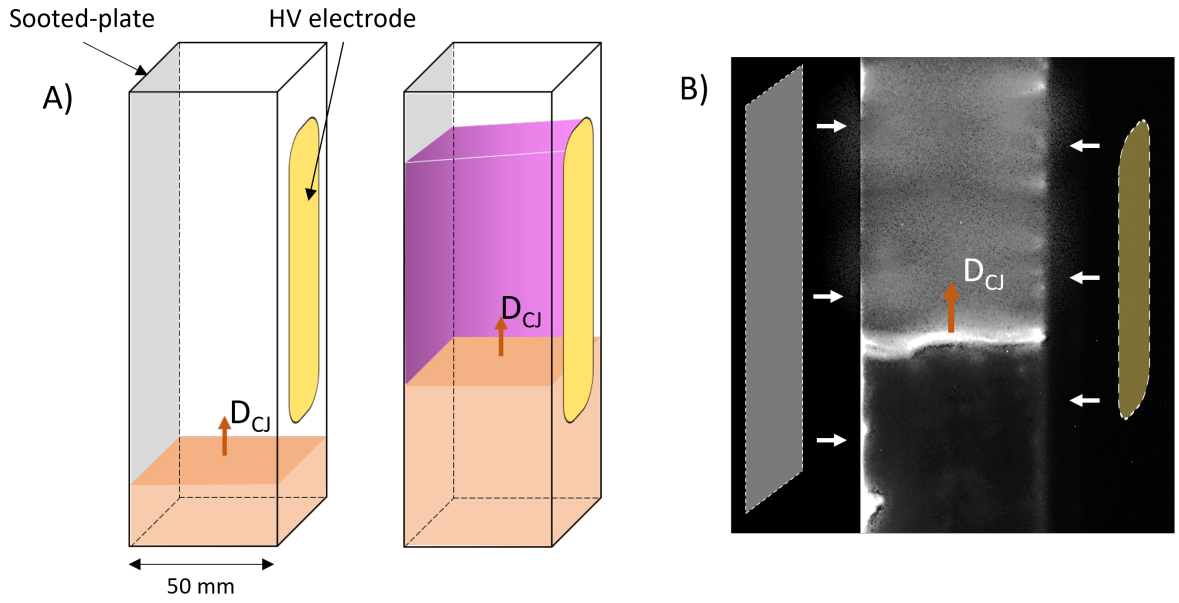

Figure 2: Schematic of the nanosecond discharge sequence. The HV and grounded electrodes are shown in yellow and grey, respectively. (A): Detonation front shown in orange. Left: before the NS discharge. Right: during the ns discharge, with the plasma shown in purple. (B): Typical ICCD image of the detonation front and plasma for H_2:O_2 = 2:1 at 120 mbar, gate=50 ns.

The diagnostic chamber had a 665 mm length, and its four walls were replaceable. The brass HV electrode (24×370 mm^2) was inserted in a dielectric (PEEK) plate mounted in a stainless steel chamber wall (Fig. 1), opposite to the grounded electrode (the sooted plate). The distance between the electrodes was L = 50 mm. The other two walls were 500 mm long borosilicate-crown glass (BK7) optical windows. Figures 2 (A) and (B) illustrate the principle of the experiment: the detonation front enters the chamber at the Chapman-Jouguet (CJ) regime velocity and the discharge is triggered at a chosen position. The detonation tube had a 200 mm long horizontal section and a 1570 mm long curved section, giving a total length at the chamber entrance of 3570 mm. Under the conditions of the present work, the curved section had no effect on the propagation of the detonation because its radius of curvature was much larger

than the widths of the detonation cells by a factor of at least 40, e.g. [44].

A standard automotive spark plug positioned at the end of the tube opposite the chamber entrance ignited the combustible mixture with deposited energy of about 50 mJ. A Shchelkin spiral then enhanced the deflagration-to-detonation process, so the detonation was self-sustained before entering the curved section of the tube. Six pressure transducers, similar to those in the chamber, were mounted along the horizontal part of the tube to ensure that the CJ regime was achieved at the detonation entry to the chamber. Two others were mounted opposite each other at the chamber entrance to ensure that the detonation front was symmetrical relative to the chamber axis.

The fresh reactive mixtures were prepared in advance in a mixing unit and then stored in a 4 bar tank adjacent to the test bench. The detonation tube and diagnostic chamber were pre-vacuumed to less than 0.2 mbar prior to injection of the fresh reactive mixture. This procedure ensured the same composition in each series of tests. Ignition was triggered within 5 seconds of the injection procedure reaching the initial target pressure. Table 1 shows the mixtures studied, all of which were stoichiometric.

Table 1: Composition of the gas mixtures

Mixture	Composition
CH_4:O_2:Ar	1:2:4.5
H_2:CH_4:O_2:Ar	3:2:7:18
H_2:O_2:Ar	2:1:2
H_2:O_2	2:1

A PiMax-2 ICCD camera (Princeton Instrument) was used to record the discharge for all the experiments. Figure 2 (B) shows the synchronization of the detonation front with plasma. After the detonation initiation, the triggering sequence was started by using the signal from the first pressure transducer detecting the detonation front (P1, Fig. 1) to trigger the delay generator, which then triggered the ICCD camera and the high-voltage generator. Synchronization took into account the travel times of the detonation front in the detonation tube and the high-voltage signal in the cable. The images were integrated over the spectral range of 200-900 nm, the ICCD gate was equal to 350 ns, and the typical uncertainty in the position of the front was $\pm$ 10 mm.

A high-voltage generator (FPG 25-001NM2C2, FID GmbH) was designed to deliver a burst of three nanosecond pulses of negative polarity with a programmable delay between pulses from 200 ns to 2 ms. The generator impedance was low to provide the reflections of the pulse and to maximize the energy delivered to the discharge cell. The

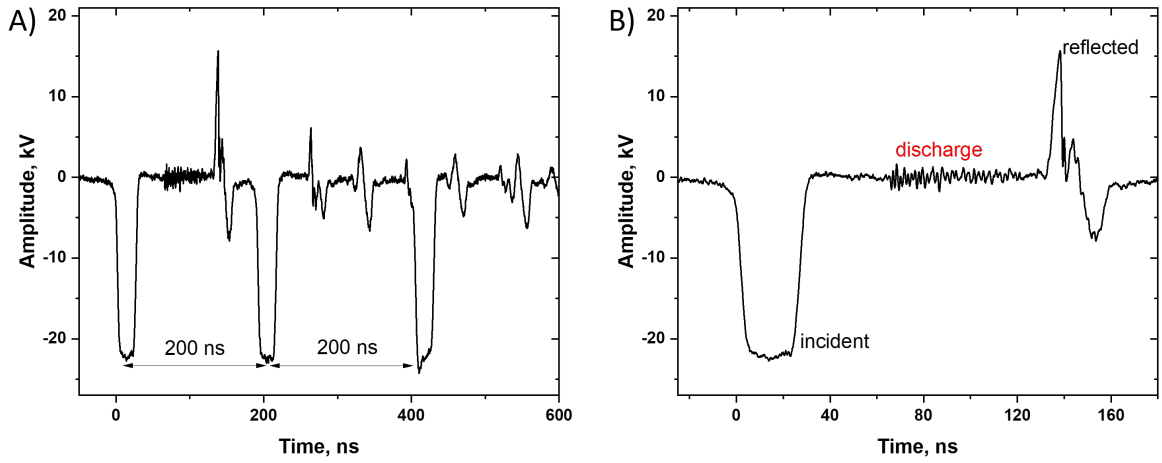

Figure 3: Waveform of the voltage measured by back current shunt in the HV cable. (A): full discharge composed of three 25 ns HV pulses spaced by 200 ns. (B): Zoom on the first pulse. Each incident pulse is reflected into the HV cable at the high voltage electrode, generating plasma in the volume.

back current shunt (BCS) technique [45] was used to measure the voltage in the cable and on the high-voltage electrode, as well as the current and the deposited energy in the plasma. A custom-made calibrated back current shunt was soldered to the shield of a 30-m long coaxial high-voltage cable connecting the generator to the diagnostic chamber.

Figure 3 shows the back current shunt signal recorded with a WaveRunner 4Xi-A 600-MHz oscilloscope (Lecroy). A burst of three pulses with a minimum time delay between the pulses of 200 ns was chosen for the experiments. The number of pulses, their amplitude and the delay between them were determined with a preliminary study for optimizing both the discharge homogeneity and the deposited energy without igniting the mixture by the plasma. The maximum amplitude of the pulses was -25 kV in the cable and -50 kV at the HV electrode (because of the superimposed forward and reflected voltage at the mismatched load). The electromagnetic noise on the BSC data is minimized as long as the discharge initiates strictly between the incident and the reflected pulses arriving at the back current shunt (Fig. 3). The first reflected pulse undergoes a sign change, indicating the closing of the gap between the electrodes, and experiences a reduction in amplitude as it is partially absorbed. Subsequent reflected pulses are mostly absorbed.

Figure 4 shows ICCD images capturing the three pulses, as well as the overall optical plasma emission throughout the discharge. The figure also shows a typical waveform from the back current shunt superimposed with the gate of the ICCD camera. The gates P_i, $i = 1 - 3$ correspond to the Pi pulses coming to the discharge chamber because the

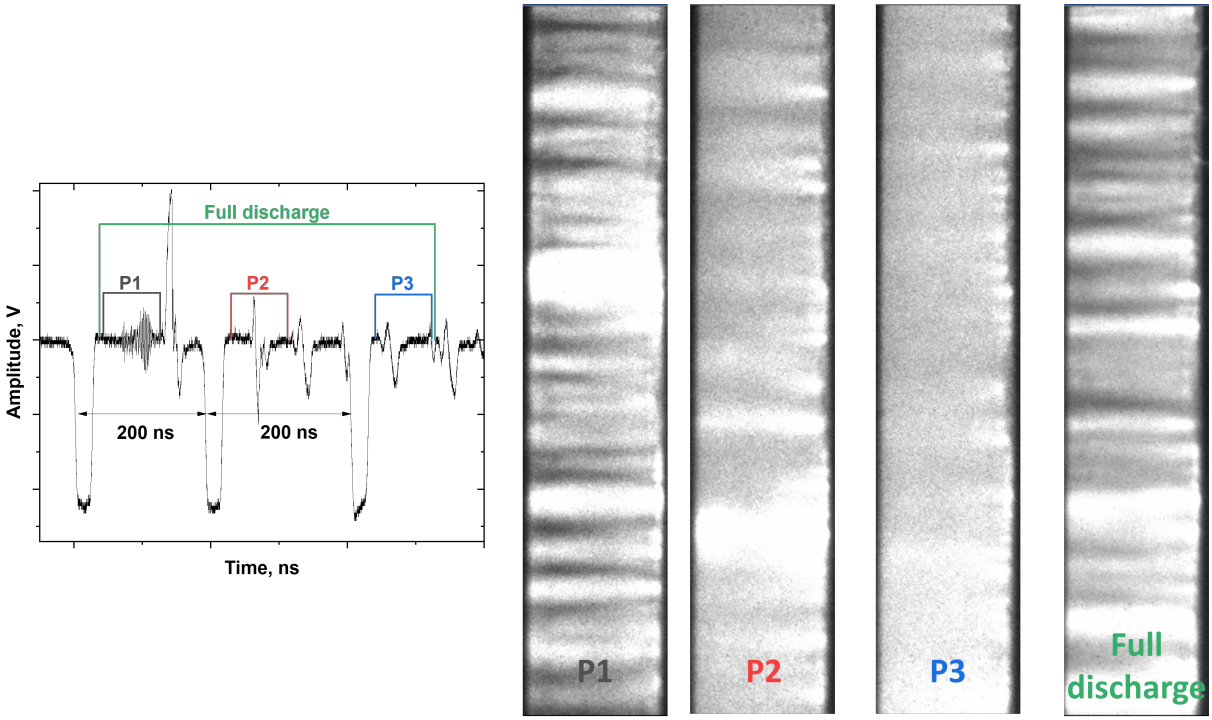

Figure 4: ICCD images of the plasma for the pulses P1, P2, P3 and the full discharge for H_2:O_2:Ar = 2:1:2 at 150 mbar. The camera gate is 200 ns for each pulse. The camera gain is the same for all recordings.

back current shunt was installed in the middle of the long cable between the HV generator and the discharge (diagnostic) chamber. The optical emission of the plasma during the first pulse exhibits a non-homogeneous structure characterized by brighter zones. In contrast, the emission from the subsequent two pulses appears more diffuse and homogeneous. A volumetric plasma with somewhat brighter zones is observed throughout the entire discharge. This information was taken into account when analyzing the data, but no correlation was found between the position of the brighter emission zones and a local reduction in cell size.

The plasma parameters were highly reproducible. The pulses delivered from the generator were identical within 0.1% of amplitude. The measured current and the delivered energy were reproducible within a few percent from shot to shot. ICCD images demonstrated stochastic non-homogeneities in the first pulse but quite homogeneous plasma in the second and the third pulses.

The measurements of the detonation velocities and the recordings of the cellular structure were highly reproducible for all mixtures and initial pressures considered. The measured velocities were equal to the CJ velocities calculated with the NASA CEA computer program [46] to within a total uncertainty of $\pm$ 80 m/s. The cell patterns were analyzed for each mixture and initial pressures. Figure 5 shows the classic effects

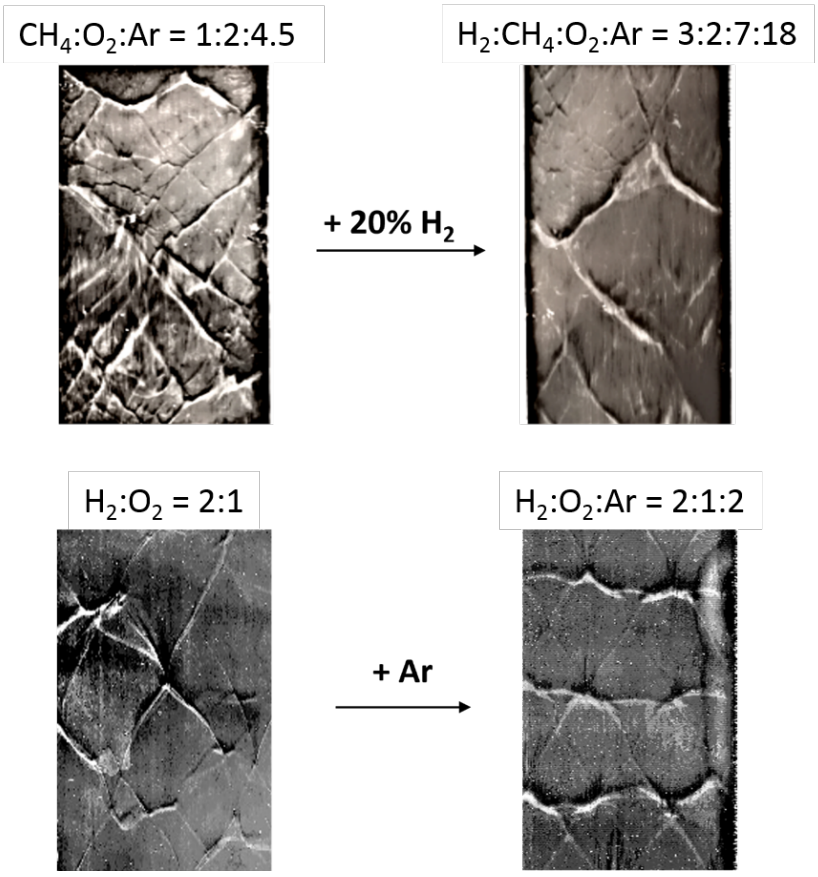

Figure 5: Effect of the mixture composition on the cellular structure and regularity. The top pair is for mixtures with CH_4 as part of the fuel mixtures, at the initial pressure of 180 mbar. The bottom set is for mixtures with H_2 as the fuel, at the initial pressure of 180 mbar150 mbar.

of hydrogen addition and argon dilution on the detonation cellular structure, i.e. the most regular cell pattern is obtained for the mixtures that contain hydrogen and are diluted with argon. The reduction in cell size due to the plasma action was observed for all mixtures but with various uncertainties depending on the composition of the mixture.

Significant attention was paid to the effect of the initial pressure of the fresh gases on plasma uniformity. For each mixture and each HV generator parameter, a pressure threshold exists above which plasma is no longer uniform. In this case, bright and thin channels (filaments) contain the major part of the discharge energy. However, the lower the pressure, the more diffuse the discharge and the more uncertain the cell recordings. Therefore, it was necessary to find the right balance between minimizing channelling and maximizing uniformity to improve the observability of the phenomenon in the soot recordings, as summarized in Figure 6.

3. Numerical approach

The aim of the numerical modelling was to relate the plasma effect to the change in cell mean width. As discussed in Section 1, predictive calculations of cell size, if relevant, remain a challenge. However, to a reasonable extent, this width is proportional to a ZND characteristic length. Therefore, the principle of the analysis is to calculate the ZND length rather than the cell width and to check that the changes are approximately in the same ratio as those in the measured cell width. Since the characteristic time of energy delivery by HV discharge to the fresh gas ahead of the detonation front (a few ns) is much shorter than the cellular and hence ZND combustion times (a few ms), the numerical approach consisted of two steps. The first step was to calculate the chemical composition of the fresh gas modified by nanosecond discharge and, in particular, the time evolution of the densities of the active species in plasma. The second step was to calculate the ZND profiles using this modified chemical composition as input.

3.1. The ZND reaction zone

The Zel'dovich-von Neumann-Döring (ZND) model of the detonation reaction zone is now accepted as the average of the cellular reaction zone when the number of detonation cells on the detonation front is large enough. The ZND reaction zone is a one-dimensional planar (laminar) steady and adiabatic flow behind a leading shock that initiates the chemical reactions. Given the initial state, the solution to this flow gives the profiles of the variables and the detonation velocity, depending on the condition chosen at the reaction zone end, i.e. sustained (subsonic, piston-driven) or self-sustained

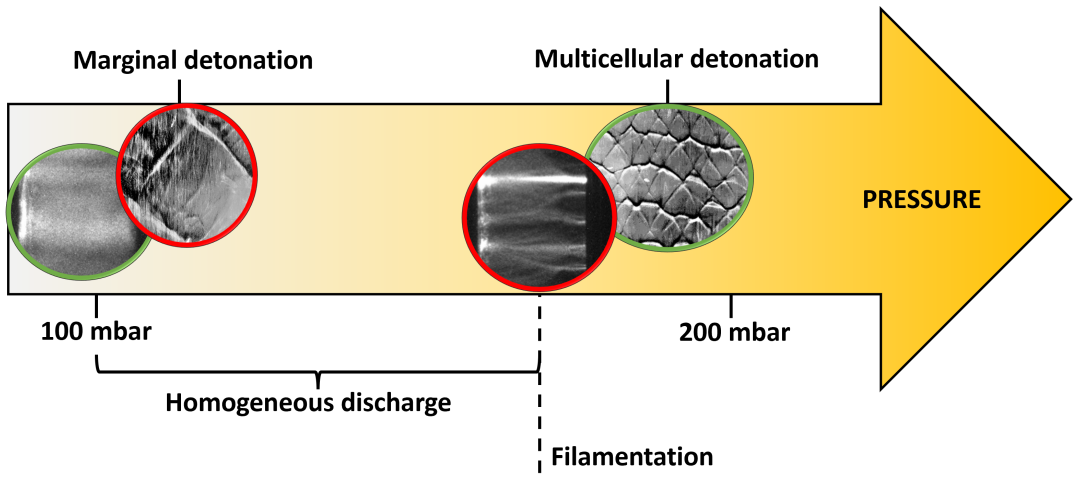

Figure 6: Combined effect of the plasma and the initial pressure on the cellular structure. Low pressures (left): the plasma is homogeneous but the detonation may be marginal. High pressures (right): the detonation is multi-cellular but plasma may show filaments. The observation conditions depend on the mixture composition and the HV generator parameters.

(sonic), similar to the Chapman-Jouguet model. The model equations are available in several reviews, e.g. [16, 26], and are not reproduced here.

The key element of a ZND calculation is the scheme that models the chemical kinetic mechanism. The induction and main-reaction thicknesses are highly sensitive to the scheme, as are the cell patterns in 3D simulations. Other things being equal, these lengths are also very sensitive to the initial composition, which also justifies the principle and the methodology retained in this analysis. The calculations in this work have been performed using the Caltech code implemented with Mevel's mechanism [47].

3.2. Kinetic model for dissociation by plasma

The time evolution of plasma species was calculated in 0D approximation. The species considered in the simulation were electronically excited Ar atoms, electrons, excited O_2 molecules, O and H atoms as well as positive ions of these elements. Negative ions were not considered because of the low rates of attachment reactions for high electric fields. The dominant process for the following ignition was dissociation of molecules. Vibrational kinetic was neglected and electronic excitation of O_2 and Ar were considered similar to [34]. The excitation of the metastable Herzberg $O_2(A^3\Sigma_u^+, C^3\Delta_u, c^1\Sigma_u^-)$ states was simulated by the excitation of one effective metastable state with an excitation energy of 4.5 eV (refered to as O_2*). The excitation of the electronic states of O_2 with higher excitation energy led to dissociation and these processes were referred to as electron impact dissociation of O_2. Excitation of electronic Ar states was simulated by the excitation of one effective state Ar* with an excitation rate being equal to the total rate of excitation of all electronically excited Ar states. In plasma-assisted combustion or detonation, the addition of a monoatomic gas such as Ar is not neutral because (i) it increases the electron average energy and (ii) the electronic excitation of Ar causes additional dissociation due to collisions with molecules. Table 2 shows the reactions and their rate constants used to calculate the production of active species in the H_2:O_2:Ar = 2:1:2 and H_2:O_2 = 2:1 mixtures. The processes considered are electron-impact dissociation, excitation and ionization, quenching of excited species, charge exchange, and dissociative recombination. The electron-impact reaction rates were calculated using the electron energy distribution function in the two-term approximation solved by the BOLSIG+ code [53]. Only collisions of electrons with the dominant neutral components (H_2, O_2 and Ar) were considered, neglecting minor species. Self-consistent sets of cross sections for elastic and inelastic electron collisions with O_2 [54], Ar [55, 56] and H_2 [57] were used.

The balance equations governing the evolution of species densities during the discharge were solved using the ZDPlaskin code [58]. The input data was the measured evolution of the reduced electric field $E/N(t)$, E is the electric field and N is the gas number density. A very short, a few nanoseconds, and high, up to a few kTd

Table 2: The kinetic scheme for dissociation by plasma

Number	Reaction	Rate constant*)	Ref
Dissociation			
R1	$e + H_2 \rightarrow e + 2H$	$f(E/N)$	text
R2	$e + O_2 \rightarrow e + 2O$	$f(E/N)$	text
Excitation			
R3	$e + O_2 \rightarrow e + O_2^*$	$f(E/N)$	text
R4	$e + Ar \rightarrow e + Ar^*$	$f(E/N)$	text
Ionization			
R5	$e + H_2 \rightarrow 2e + H_2^+$	$f(E/N)$	text
R6	$e + O_2 \rightarrow 2e + O_2^+$	$f(E/N)$	text
R7	$e + Ar \rightarrow 2e + Ar^+$	$f(E/N)$	text
Quenching			
R8	$O_2^* + H_2 \rightarrow O_2 + 2H$	1.0×10^{-10}	[48]
R9	$Ar^* + H_2 \rightarrow Ar + 2H$	7.0×10^{-11}	[49]
R10	$Ar^* + O_2 \rightarrow Ar + 2O$	2.0×10^{-10}	[49]
Charge exchange			
R11	$H_2^+ + H_2 \rightarrow H_3^+ + H$	2.1×10^{-9}	[50]
R12	$H_2^+ + O_2 \rightarrow HO_2^+ + H$	1.9×10^{-9}	[50]
R13	$H_3^+ + O_2 \rightarrow HO_2^+ + H_2$	6.0×10^{-10}	[50]
R14	$HO_2^+ + H_2 \rightarrow H_3^+ + O_2$	3.0×10^{-10}	[50]
R15	$O_2^+ + H_2 \rightarrow HO_2^+ + H$	4.0×10^{-11}	[50]
R16	$Ar^+ + H_2 \rightarrow Ar + H_2^+$	7.1×10^{-10}	[51]
R17	$Ar^+ + O_2 \rightarrow Ar + O_2^+$	1.0×10^{-10}	[51]
Recombination			
R18	$e + H_2^+ \rightarrow H + H$	$2.3 \times 10^{-7}(300/T_e)^{0.4}$	[52]
R19	$e + H_3^+ \rightarrow H + H + H$	$2.8 \times 10^{-7}(300/T_e)^{0.8}$	[52]
R20	$e + HO_2^+ \rightarrow H + O_2$	$7.1 \times 10^{-7}(300/T_e)^{0.72}$	[52]
R21	$e + O_2^+ \rightarrow O + O$	$2.4 \times 10^{-7}(300/T_e)^{0.7}$	[52]

*) Rate constants are given in cm^3/s and the temperature in K.

(1 Td= 10^{-17} V $\cdot$ cm^2), overshoot of $E/N(t)$ at the beginning of the very first pulse of applied voltage corresponds to the passage of the fast ionization wave (FIW) closing the gap and cannot be resolved by used experimental technique. To take into account the production of charged species in this overshoot, the initial electron density was considered as an initial parameter of the calculation. It was selected to provide an agreement between the calculated and measured waveforms of the discharge current and/or deposited energy. In the present calculations, this initial electron density produced in the FIW front, was taken to be equal to $6 \cdot 10^9$ cm^{-3}.

4. Results and discussion

Several phenomenon resulting from a HV nanosecond discharge influence chemical composition and combustion process. They are (i) the generation of active species [31], (ii) an increase in gas temperature due to the relaxation of energy stored in electronically excited species (fast gas heating, FGH) [59, 60] and vibrational-translational (VT) relaxation [59], (iii) hydrodynamic effects [61–63]. A quantitative analysis of the plasma parameters on a nanosecond time scale is essential to understand how plasma can modify the cell widths.

Below, Subsection 4.1 presents the experimental observations based on soot recordings of the responses of the cell structure to the plasma action. Then, Subsection 4.2 presents the measured discharge current, reduced electric field and specific energy deposition (SED). They are used as input data and criteria for numerical calculations as well as for the estimate of the heat release due to the discharge. Finally, Subsection 4.2 presents the calculated dissociation degrees of the fresh gas, i.e. the plasma-induced fresh composition. They are used as input to calculations of changes in ZND characteristic lengths, and hence of cell widths (Sect. 1).

4.1. Experimentally measured reduction of the cell size

Figure 7 shows three soot recordings of cellular structures for the mixture H_2:O_2:Ar = 2:1:2 at 150 mbar obtained without plasma (plate A), with plasma triggered at time t_0 (plate B), and with plasma triggered at time $t_1 = t_0 + 0.25$ ms (plate C). The letter P indicates the zones where plasma was generated. The red arrow indicates the direction of propagation of the detonation front.

Two regimes of detonation propagation can be identified. The first one is the reference case because it is observed without plasma, i.e. on the whole plate A and before plasma application on plates B and C. The corresponding cells have a mean width $\lambda \simeq 1.6$ cm, a typical value for this mixture with argon dilution ranging from 55.6% [64] to 70% [65] at 150 mbar. The second regime is only observed in the plasma zones of plates B and C. The corresponding cells have a mean width $\lambda \simeq 0.75$ cm, half that of the reference regime. The cell modification starts at the exact time and position where the discharge occurred, t_0 for plate B and t_1 for plate C. This demonstrates the instantaneous adaptation of the cellular structure to the plasma action, compared to the characteristic propagation time of the front. Similar observations were made in [42, 43], with initial states subject to gradients of the equivalence ratio parallel to the propagation direction. The changes in the cells can be more evidently seen from the enlargements presented in Figure 8. The selected zones are marked “1” on the plate A for the reference regime (without plasma) and “2” on the plate C for the other (with plasma). The schematics to the right of the enlarged images highlight the interaction of the transverse waves moving parallel to the soot plate (y-axis), i.e. the cells, as dark lines, and the impact of the transverse waves normal to the plate (x-axis) as white lines.

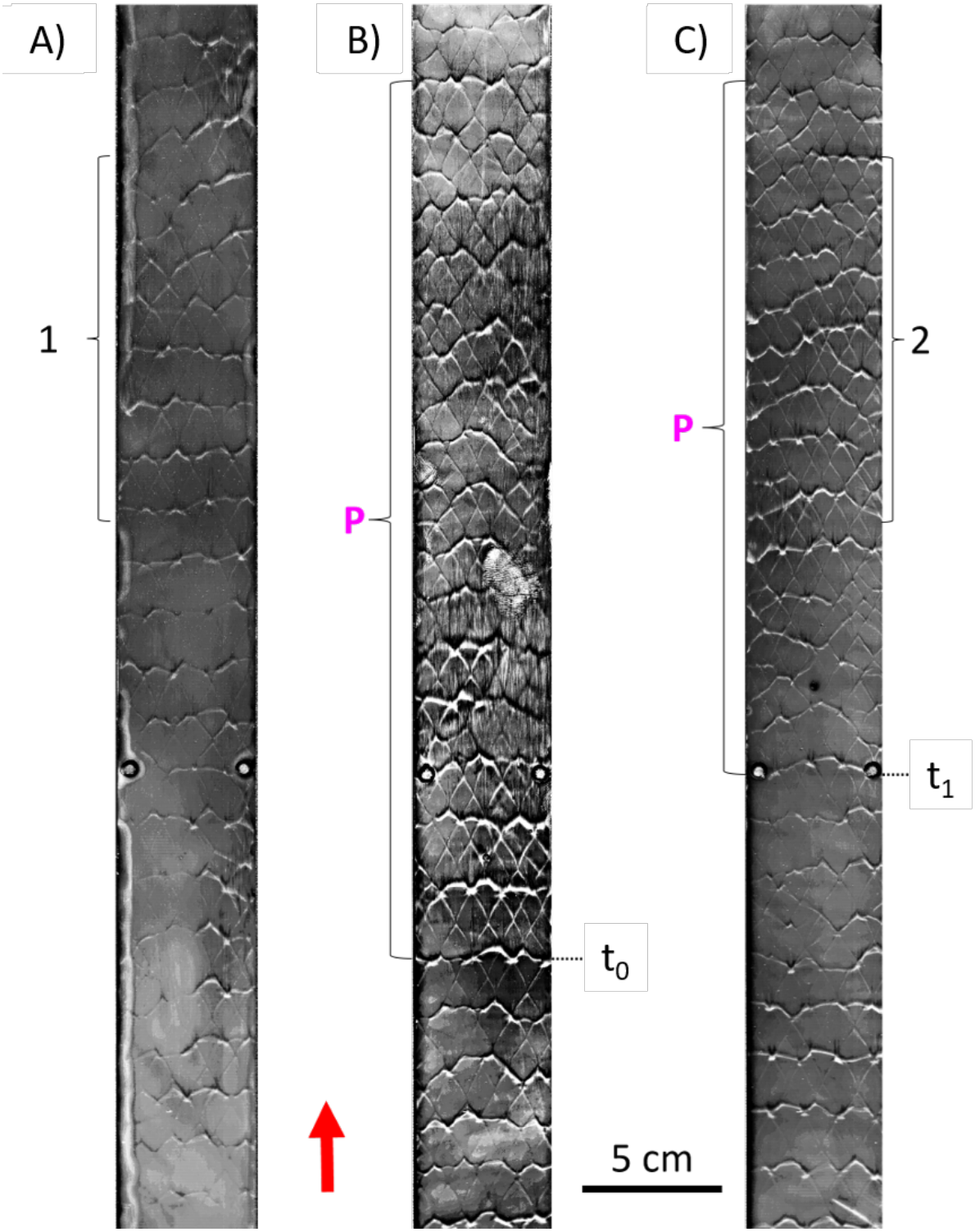

Figure 7: Cellular structure for H_2:O_2:Ar = 2:1:2 at 150 mbar. Plate A: no plasma; Plate B: plasma triggered at time t_0; Plate C: plasma triggered at time $t_1 = t_0 + 0.25$ ms.

Thus, for H_2:O_2:Ar = 2:1:2, the plasma effect is a reduction in the mean width of the cells by a factor of about 2 and an increase in their irregularity, also indicated by the

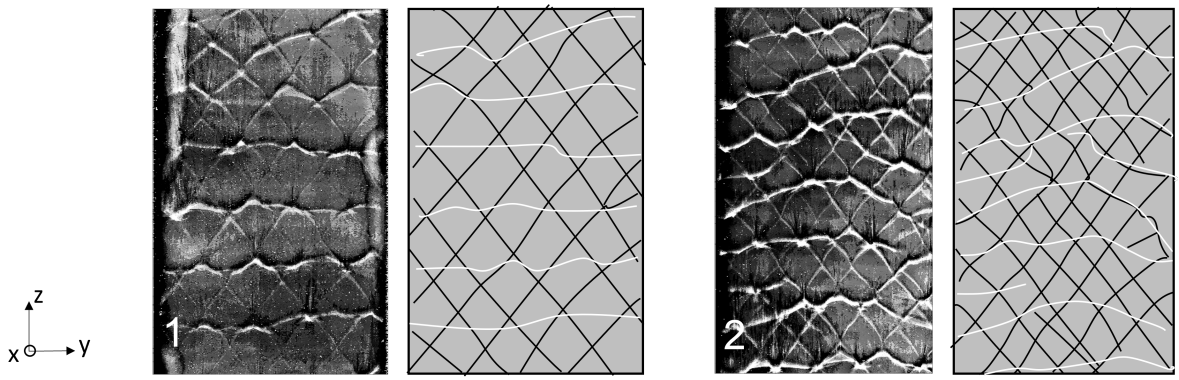

Figure 8: Zoomed views for H_2:O_2:Ar = 2:1:2 at 150 mbar. The left and right pairs show the soot recordings and their schemes of the transverse wave tracks for zones 1 and 2 in Figure 7, respectively.

accentuation of the unevenness of the transverse impact lines.

Figures 9 and 10 show identical qualitative trends for the undiluted mixture H_2:O_2 = 2:1 at 120 mbar, using the same notation as in Figures 7 and 8. The differences are (i) reference cells less regular than for the diluted mixture (plates A, no plasma); (ii) higher reduction in cell width, i.e. by the greater factor of 2.75; (iii) no significant change in cell regularity. The reduction in cell size is more evident in the enlargements shown in Figure 10. For the reference regime, the cell mean width is $\lambda \simeq 1.8$ cm, which is the typical value for this mixture at 120 mbar [66,67]. For the second regime, the cell mean width in the plasma zone of plate B is $\lambda \simeq 0.65$ cm.

The same experiments and analysis were conducted for each of the mixtures listed in Table 1, with the initial pressures ranging from 120 to 200 mbar. Figure 11 shows the experimental cell width reduction factor as a function of the initial pressure. Its mean value is approximately two, and the plasma efficiency in reducing the cell width increases with decreasing pressure. The uncertainties on λ represented by error bars were estimated by considering the number of plates, the cell pattern regularity, and the number of cells per plate section. The results of calculations presented in the same figure, are discussed in Sub-section 4.3.

4.2. Measured plasma parameters and estimates of gas heating

The specific energy delivered to the plasma under the conditions of the present experiments is low, $\omega \approx 3 \cdot 10^{-3}$ eV/mol. Since no correlation was observed between brighter discharge zones and a local reduction in detonation cell size, possible local hydrodynamic effects related to higher energy release in brighter zones were excluded from further consideration. The action of plasma was assumed to be uniformly volumetric over the discharge gap.

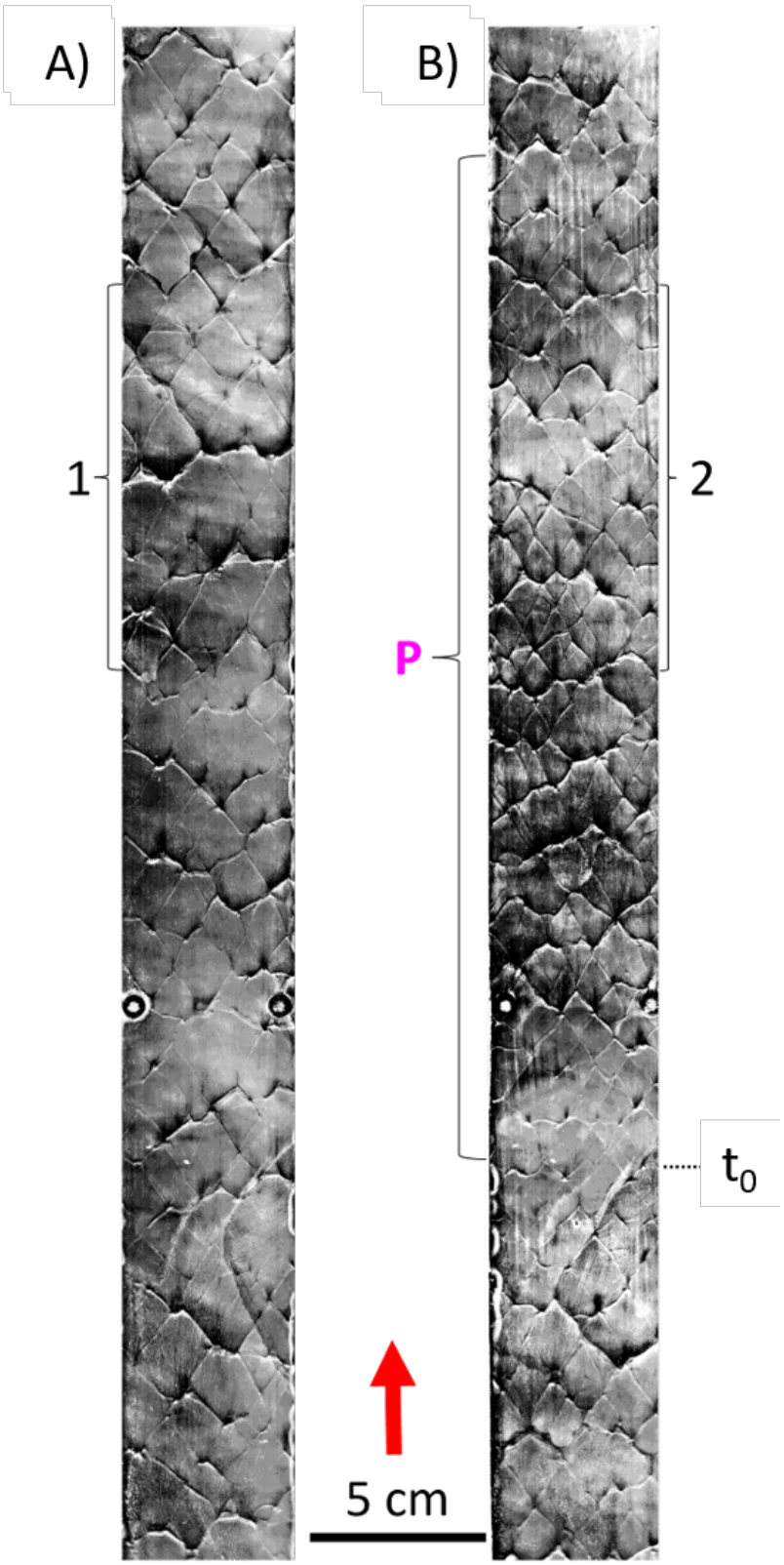

Figure 9: Cellular structure for H_2:O_2:Ar = 2:1 at 120 mbar: Plate A: no plasma; Plate B: plasma triggered at time t_0.

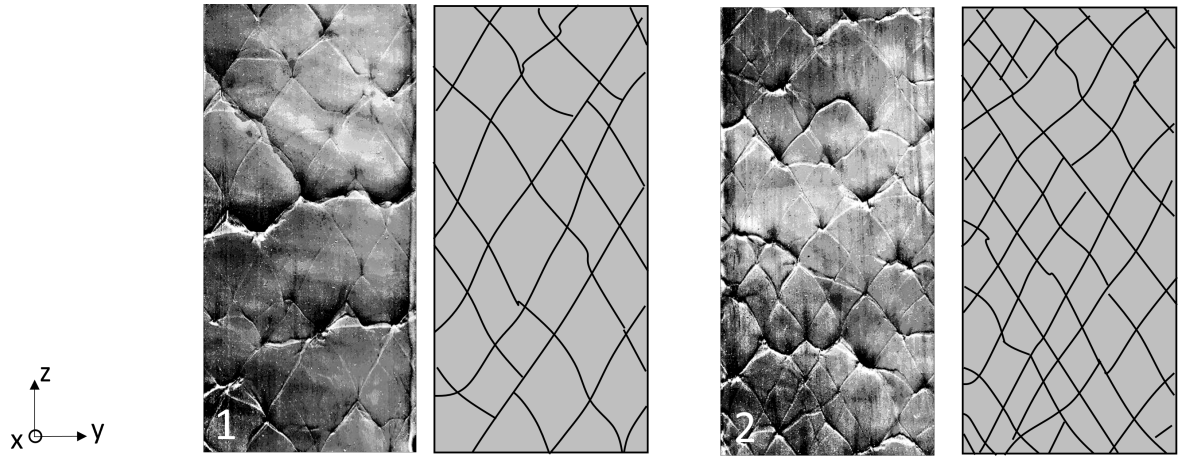

Figure 10: Zoomed views for H_2:O_2 = 2:1 at 120 mbar. The left and right pairs show the soot recordings and their schemes of the transverse wave tracks for zones 1 and 2 in Figure 9, respectively.

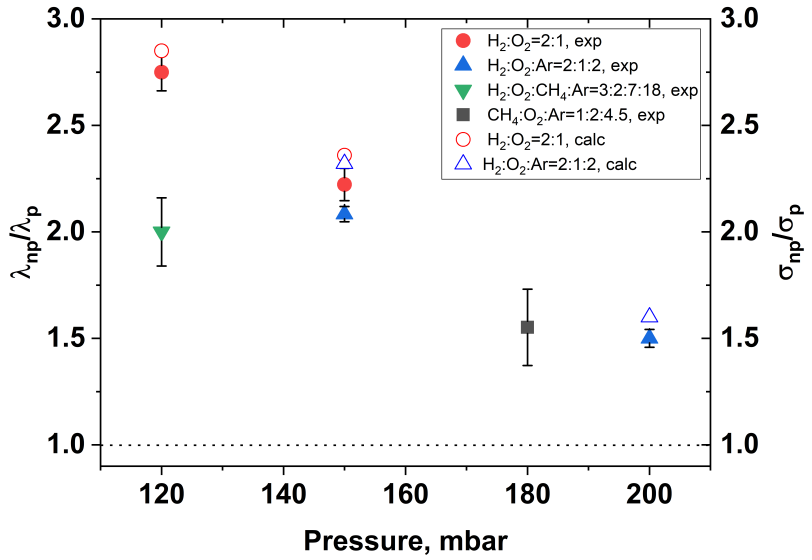

Figure 11: Cell width (left) and ZND length (right) reduction factors as a function of initial pressure. Full symbols: experimental results, open symbols: calculation results. Designations λ_p, σ_p: with plasma; λ_{np}, σ_{np}: without plasma.

The measurements of electrical parameters presented below are necessary to estimate the respective contributions of FGH and VT–relaxation to the fresh gas heating. The experiments were carried out in H_2:O_2:Ar = 2:1:2 mixture at 150 mbar. They serve to estimate the respective contributions of FGH and VT–relaxation to the fresh gas heating.

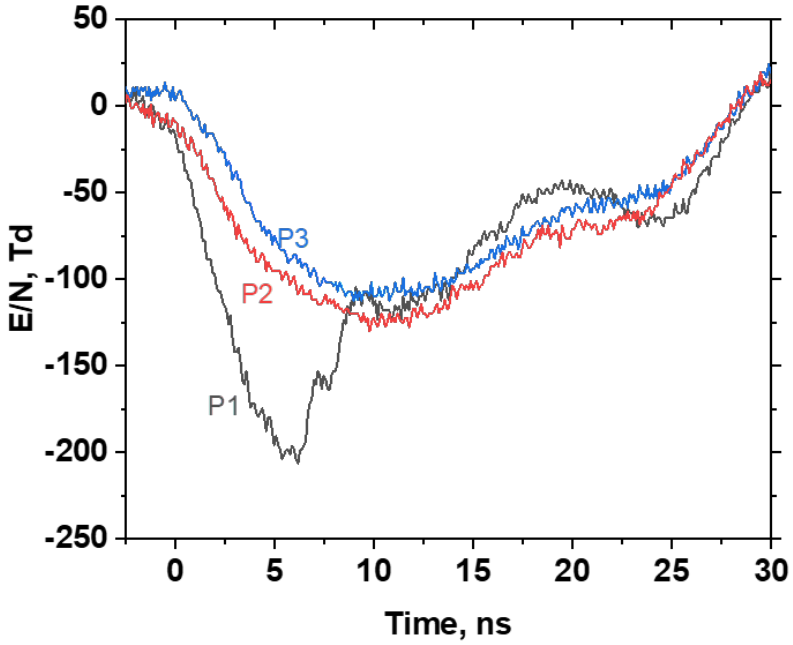

Figure 12: Reduced electric field measured by back current shunt for the three pulses P1, P2 and P3 for H_2:O_2:Ar = 2:1:2 at 150 mbar.

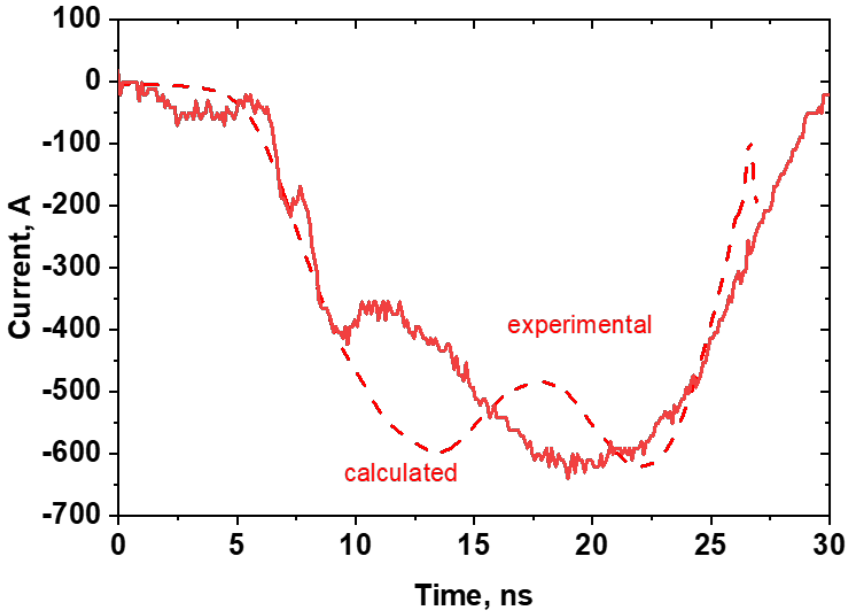

Figure 13: Waveforms of the measured (solid line) and calculated (dashed line) electrical current for H_2:O_2:Ar = 2:1:2 at 150 mbar.

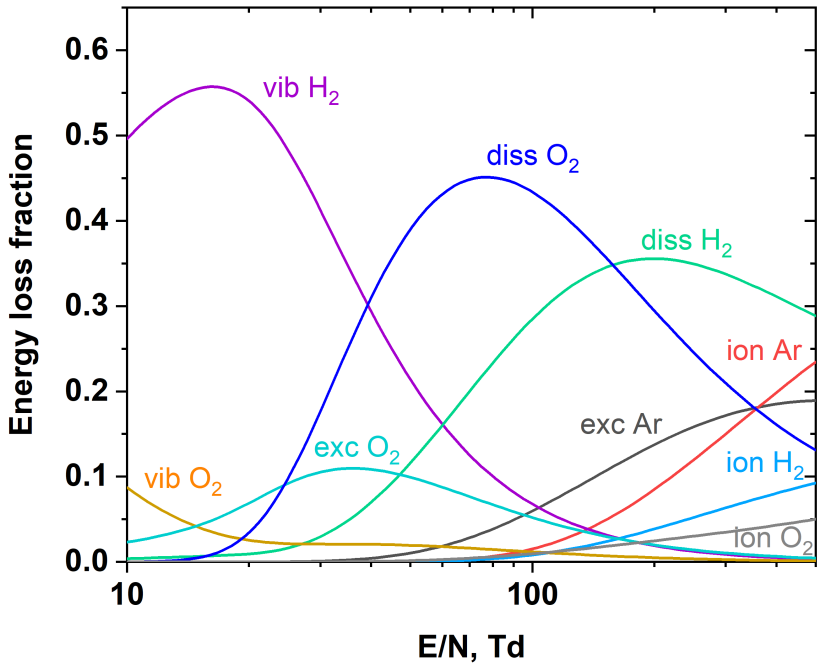

Figure 14: Energy loss fraction *vs* reduced electric field in H_2:O_2:Ar = 2:1:2 at 150 mbar.

Figure 12 shows the electric field averaged over the discharge gap and reduced by the back current shunt. The $E/N(t)$ was determined by calculating the voltage difference $U(t)$ between the electrodes divided by the distance between the electrodes L and then normalized to the gas number density N. The three high-voltage pulses are ordered from 1 to 3, corresponding to the time t, $t+200$ ns and $t+400$ ns, respectively. The first pulse (P1) generates values of E/N that decrease from 200-225 Td to a plateau between 125 and 75 Td. The second (P2) and third (P3) pulses generate no peak and a plateau with $E/N \approx 100$ Td.

Figure 13 illustrates the calculated and experimentally measured current waveforms for the first pulse (P1). The current was calculated from the electron density, using the so-called hydrodynamic approximation [68], $I = e \times n_e \times v_{dr} \times S$, where e and $n_e(t)$ are the electron charge and density, $v_{dr}(t) = \mu(t, E/N(t))E/N(t)$ and $\mu(t, E/N(t))$ are a drift velocity and the mobility of an electron, and S is the surface equal to the length of the high-voltage electrode multiplied by the average width of the electrodes. That provided a reasonable agreement between the calculated and measured current. The slight discrepancy observed in the interval $12-17$ ns was attributed to the possible occurrence of a second delayed breakdown due to the elongated electrode.

Measurement of the reduced electric field provides a means for analyzing the direc-

tion of the deposited energy distribution in the plasma. Figure 14 shows the calculated loss fractions of energy dissipated in different electron impact reactions as a function of E/N for the H_2:O_2:Ar = 2:1:2 mixture. This dependence is known in plasma physics as "energy branching". At low electric fields, $10-20$ Td, about 55% of the energy goes into the vibrational excitation of H_2. This channel decreases significantly with E/N, down to only 5% at 100 Td. Excitation of the electronic levels of atoms and molecules, designated in Fig. 14 as "exc Ar" and "exc O_2", starts at higher electric fields, tens of Td. Dissociation of O_2 and H_2 via electronically excited states is designated as "diss O_2" and "diss H_2" respectively. It is seen that the corresponding fractions of energy loss increase with increasing E/N up to a maximum at approximately 100 Td. The ionization of atoms and molecules becomes dominant at $E/N > 500$ Td.

The effects of FGH and VT-relaxation can be estimated from the data presented in Fig. 14.

FGH is an abrupt rise in the temperature resulting from the relaxation of electronically excited states of atoms and molecules [60]. It can be as high as thousands of Kelvin for tens of nanoseconds. In air, the fraction of the total energy delivered to the plasma by FGH can be estimated to be $\eta_R \approx$30% [60], using the typical reduced electric fields of the present work, i.e. 75 Td$< E/N <$ 125 Td. Because no detailed information on FGH is available for combustible mixtures, this value was used for the mixtures of this study, giving an estimate of $\Delta T \approx 7$ K for the fresh gas temperature increase.

VT-relaxation is slower than FGH. The rate constant for the $H_2(v)$ VTR on H_2 molecules [59] is equal to $k_{VT}^{H_2} = 1.6 \times 10^{-11} \sqrt[3]{T} \cdot exp(-100/\sqrt{T})$ cm^3/s, which gives an estimate of the characteristic time $\tau_{VT} \approx 2$ μs. This time is still much shorter than the detonation travel time through the discharge zone, $\tau_{DW} \sim 250$ μs, which means that VT-relaxation could be fast enough to provide the gas heating. However, Figure 14 shows that the part of the energy that goes to the vibrational excitation does not exceed 5% at $E/N = 100$ Td, which is 6 times smaller compared to FGH input. The vibrational energy of H_2 can also be spent on dissociation enhancement [69], further reducing any possible contribution to heating.

Thus, the estimated increase in initial temperature appears to be too small, i.e. $\lesssim \mathcal{O}(10)$ K, to significantly heat the fresh gas under the conditions of this work. From such small increase, the Rankine-Hugoniot relations, given the post-shock equation of state and a representative shock velocity for detonation, i.e. 1000-3000 m/s, cannot produce large enough post-shock temperature increases (i.e. behind the forward facing fronts of the cellular structure) that could increase the chemical reaction rates enough to halve the cell width.

The effect of a given initial temperature change on cell width should also be dis-

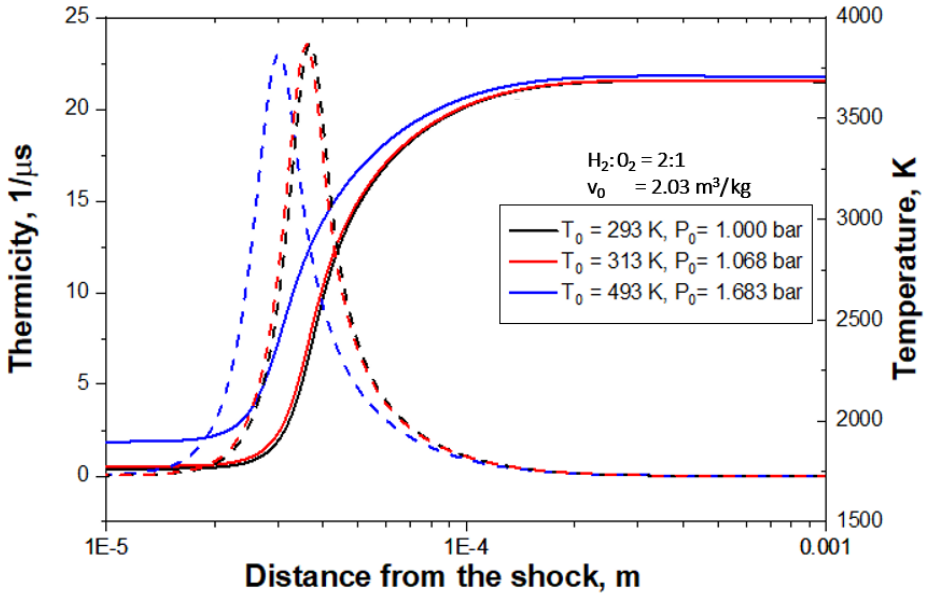

Figure 15: Effect of changes of the initial temperature (T_0) at constant initial volume (v_0) on ZND profiles of thermicity (left scale, dashed lines) and temperature (right scale, solid lines) for H_2:O_2 = 2:1.

cussed. The cell width λ depends on the initial temperature (T_0) and pressure (p_0), given the mixture composition. There is a large body of data as a function of p_0 at constant T_0, but data as a function of T_0 are scarcer because it is more difficult in gas detonation physics to vary T_0 accurately over a large enough range. For example, the available data for H_2 and several C_xH_y fuels, e.g. [9, 70], show opposite trends depending on whether p_0 or v_0 (the initial specific volume) is held constant. For constant p_0, λ increases with increasing T_0 from the ambient, reaches a maximum at about 600 K independent of the fuel, and then decreases. The lower increase is for H_2. For constant v_0, λ essentially decreases with increasing T_0 from the ambient. In particular, experiments [70] show a smaller decrease for H_2 at least until T_0 reaches about 600 K.

ZND calculations were performed to obtain data under experimental conditions comprising those of the study. Figure 15 presents the results obtained for the the mixture H_2:O = 2:1 with T_0 equal to 20°C, 40°C, and 220°C, and v_0 held constant since the discharge cannot change it. The figure shows the corresponding values of p_0. The ZND characteristic length, chosen here at the position of the thermicity maximum (Sect. 1), does not vary by more than 20%, which is significantly less than the experimental plasma-induced changes of 100-150% on cell width.

Thus, under the conditions of this study, the effects of initial temperature change can be neglected. The instantaneous reduction in cell width experimentally observed under the plasma action of a nanosecond discharge can only result from the dissociation

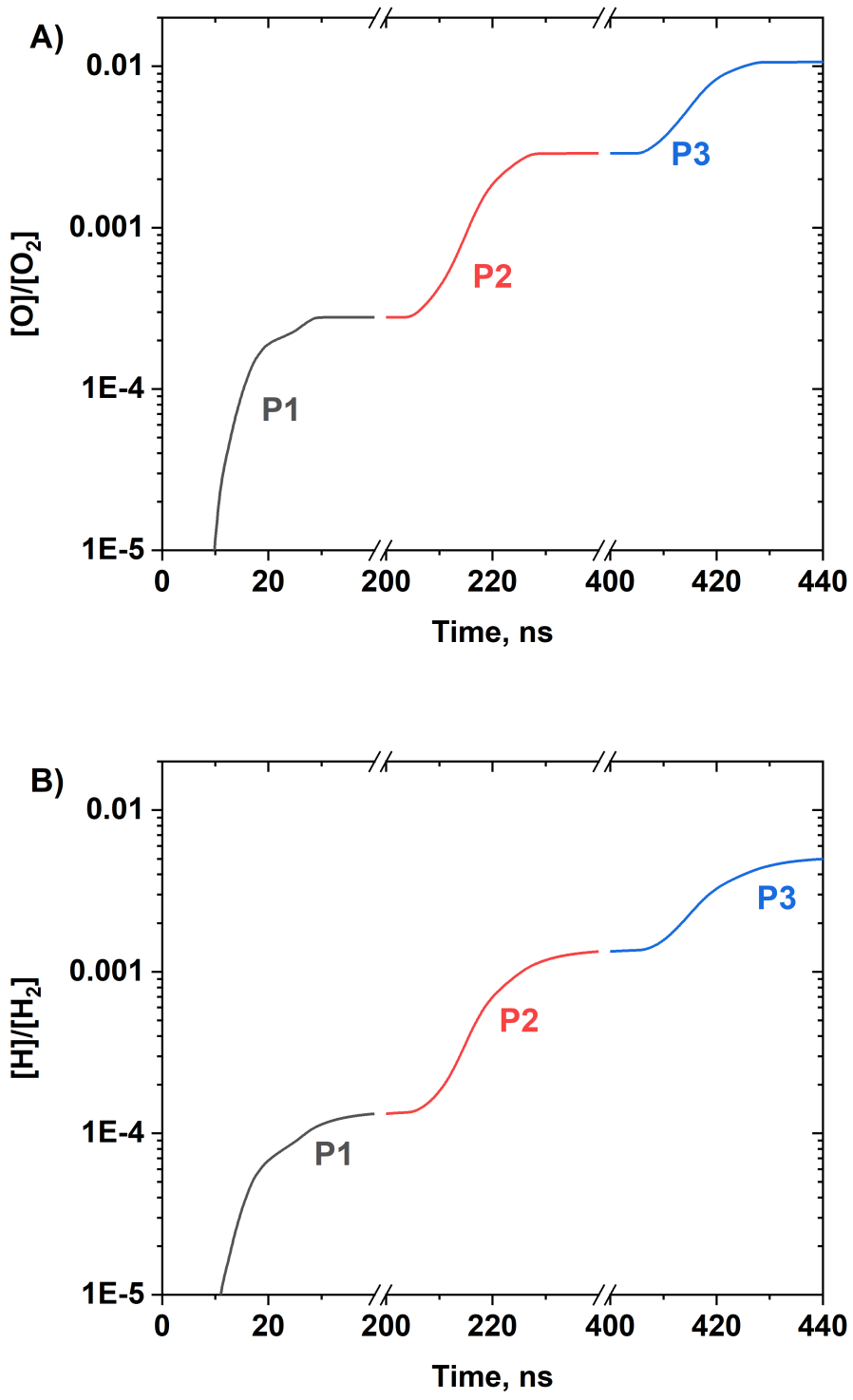

Figure 16: Evolutions of the oxygen (top, A) and hydrogen (bottom, B) dissociation degrees for the three discharge pulses in H_2:O_2:Ar = 2:1:2 at 150 mbar.

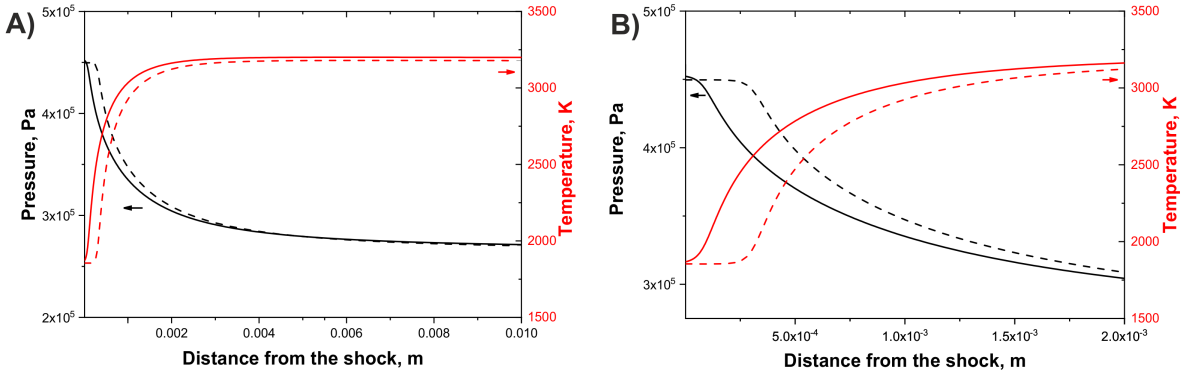

Figure 17: Plasma effect on the ZND profiles of temperature (red lines) and pressure (black) profiles for H_2:O_2:Ar = 2:1:2 at 150 mbar. Dashed lines: without plasma. Solid lines: with plasma. Left (A): linear distance scale. Right (B): log distance scale.

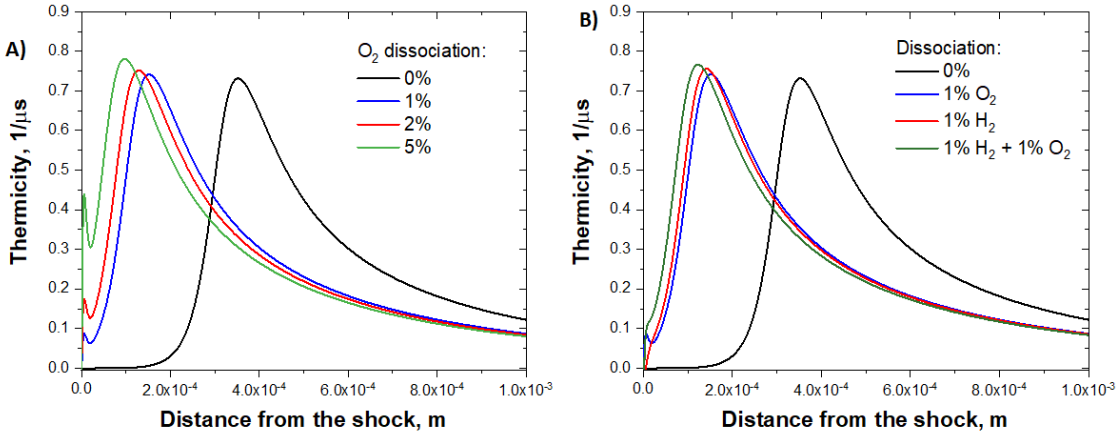

Figure 18: Effect of O_2 and H_2 dissociation in plasma on the ZND profiles of thermicity for $2H_2$:O_2:2Ar = 2:1:2 at 150 mbar. (A) oxygen molecule alone. (B) oxygen and hydrogen molecules.

of O_2 and H_2 molecules, which is analyzed below.

4.3. Dissociation in the discharge and influence of initial O-atoms density on ZND calculations

All results presented in the paper are for the mixture H_2:O_2:Ar = 2:1:2 at 150 mbar. Figure 16 presents the oxygen and hydrogen dissociation degree calculated using the kinetic scheme presented in Subsection 3.2. The dissociation degree increases progressively during each discharge pulse. Pulse 1 is mainly responsible for the breakdown and the initial ionization in the discharge zone, while O-atoms are produced mainly in the pulses 2 and 3. Since (see Figure 4) the plasma is more spatially homogeneous

in pulses 2 and 3, the fact that the majority of atomic oxygen is produced in these pulses explains the homogeneity of the cellular structure modification on the scale of the plasma zone. Finally, dissociation degree reaches about 1% for oxygen and 0.44% for hydrogen at 400 ns. These values represent estimates of the maximum density of atoms observed under the experimental conditions presented in this paper. They have been used as initial parameters for the ZND calculations (Sect. 3).

It is important to note that at room temperature, the characteristic time of atomic density decay due to combustion reactions is long, significantly longer than the time of passage of the detonation wave through the plasma zone. The fastest recombination process for O atoms at 150 mbar is a three-body recombination with ozone production, with a characteristic time being equal to 250 microseconds. This time is smaller but comparable with a typical time of passage of the detonation wave (1780 m/s) through the plasma zone (0.37 m). We do not observe any progressive change in the cell size along the plasma zone, even if the part of atomic oxygen can be converted to ozone ahead of the wave during the propagation. Our explanation is that O_3 lifetime at room temperature is much longer and ozone serves as a "storage" of O-atoms but dissociates at the arrival of the detonation wave. As a consequence, not only the time of arrival of the detonation front in the discharge zone but the entire passage of the detonation wave through the plasma zone is not affected by a recombination of atomic oxygen under the conditions of the present experiment.

Figure 17 presents the pressure and temperature ZND profiles without plasma and with plasma (i.e. with the densities of oxygen and hydrogen atoms given above). With plasma, the atoms produced in the fresh gas lead to an earlier start of the exothermic reactions. As a result, the ZND temperature increase and pressure decrease are observed at a significantly lower distance from the shock. It is worth noting that at the end of the reaction zone, the thermodynamic properties are identical with and without plasma. This figure illustrates that the plasma action significantly modifies the reaction zone of the ZND model of detonation propagation.

Figure 18 shows the thermicity profiles depending on the dissociation degree of the oxygen and hydrogen molecules. Figure 18-A) shows the dissociation effect of oxygen (0, 1, 2 and 5%). A significant reduction in the ZND chemical length taken as the distance from the shock to the thermicity peak (Sect.1), that is, about a factor of 2, is observed starting from 1% of dissociation. However, the effect is not linear, as dissociation of 2% of oxygen does not lead to a significant further reduction. As the dissociation degree increases, thermicity decreases before increasing, which expresses a slower temperature rise. Figure 18-B) presents the effect of 1% dissociation of oxygen and hydrogen, independently and combined. The shortest reduction of chemical length is obtained for 1% H_2 + 1% O_2 but the difference between 1% H_2 and 1% O_2 independently is minor. The ZND chemical length of the H_2:O_2:Ar = 2:1:2 mixture is significantly

reduced, i.e. by half, just starting from a 1% dissociation of oxygen and hydrogen. The calculation results of plasma-induced ZND length reduction for H_2:O_2 and H_2:O_2:Ar mixtures are presented in Figure 11. The comparison with the experimental results shows a good agreement: the ratio of cell widths w to w/o plasma is close to the ratio of the ZND characteristic lengths.

5. Conclusions

This work demonstrates experimentally the reduction of the detonation cell size by creating a spatial region of low-temperature nonequilibrium plasma in front of a detonation wave front. The nonequilibrium plasma was created by a pulsed nanosecond high-voltage discharge synchronised with the arrival time of the wave front in the observation section of the detonation tube. The plasma was produced by a few (typically 3) high-voltage pulses, each having an amplitude of about 50 kV on the high-voltage electrode and 30 ns (FWHM) duration, with an interval of 200 ns between pulses.

Particular attention was paid to the choice of gas mixture and the range of initial pressures. Four mixtures were selected: CH_4:O_2:Ar = 1:2:4.5, H_2:CH_4:O_2:Ar = 3:2:7:18, H_2:O_2:Ar = 2:1:2 and H_2:O_2 = 2:1 at pressures ranging from 100 to 200 mbar. For all selected conditions, the relative reduction in detonation cell size ranged from 1.5 times for 200 mbar to nearly 3 times for 120 mbar, with a weak dependence on mixture and initial pressure.

Measurements of the size of the detonation cells were accompanied by measurements of the discharge current and voltage. Typical delivered energies were in the order of 10^{-3} eV per particle. The reduced electric field in the discharge, $E/N = 75 - 125$ Td, provided the most favorable conditions for the dissociation of molecules *via* electronically excited states. Based on the analysis of the characteristic times of heat release and deposited energy, together with the energy branching, it was concluded that the observed reduction in the width of the detonation cells was exclusively due to kinetics.

The compositions of the fresh gas dissociated by plasma were used as input for ZND calculations. Discharge kinetics calculations were performed based on the time dependence of the electric field, using the measured current as a reference. The results indicate that relatively low atomic densities in the fresh gas are sufficient to significantly reduce a ZND characteristic chemical length, i.e., by about the same ratio of 2 as the observed cell width reduction. This experimentally and numerically demonstrates the possibility of controlling detonability using a non-equilibrium plasma.

Acknowledgements

This work was partially supported by DGA (EP-DGA convention N2790) and by the National French Research Agency (ANR-18-EURE-0014). Work of Mr Ryu Masuda was supported by Research Program for International Talents, Institut Polytechnique de Paris. The authors express their gratitude to Dr. Sergey Shcherbanev for his valuable early contributions to this research. Additionally, special thanks are given to Ali Mahjoub and Pascal Pariset for development and production of the electrode system for the detonation tube.

References

[1] D. M. Johnson, G. B. Tomlin, D. G. Walker, Detonations and vapor cloud explosions: Why it matters, J. Loss Prev. Process. Ind. 36 (2015) 358–364.

[2] E. S. Oran, G. Chamberlain, A. Pekalski, Mechanisms and occurrence of detonations in vapor cloud explosions, Prog. Energy Combust. Sci. 77 (2020) 100804.

[3] A. Rasheed, A. H. Furman, A. J. Dean, Experimental investigations of the performance of a multitube pulse detonation turbine system, J. Propul. Power 27 (2011) 586–596.

[4] F. K. Lu, E. M. Braun, Rotating detonation wave propulsion: experimental challenges, modeling, and engine concepts, J. Propul. Power 30 (2014) 1125–1142.

[5] K. Kailasanath, Review of propulsion applications of detonation waves, AIAA J. 38 (2000) 1698–1708.

[6] K. Kailasanath, Recent developments in the research on pulse detonation engines, AIAA J. 41 (2003) 145–159.

[7] P. Wolanski, Detonative propulsion, Proc. Combust. Inst. 34 (2013) 125–158.

[8] Y. N. Denisov, Y. Troshin, Pulsating and spinning detonation of gaseous mixtures in tubes, Dokl. Akad. Nauk. 125 (1959) 110–113.

[9] A. A. Vasilév, Dynamic parameters of detonations, in: F. Zhang (Ed.), Shock Waves Science and Technology Library, Vol. 6: Detonation Dynamics, Springer Berlin Heidelberg, 2012, pp. 213–279.

[10] D. Desbordes, H.-N. Presles, Multi-scaled cellular detonation, in: F. Zhang (Ed.), Shock Waves Science and Technology Library, Vol. 6: Detonation Dynamics, Springer Berlin Heidelberg, 2012, pp. 281–338.

[11] M. I. Radulescu, G. J. Sharpe, C. K. Law, J. H. S. Lee, The hydrodynamic structure of unstable cellular detonations, J. Fluid Mech. 580 (2007) 31–81.

[12] J. H. Lee, The detonation phenomenon, Cambridge University Press, 2008.

[13] J. Crane, J. T. Lipkowicz, X. Shi, I. Wlokas, A. M. Kempf, H. Wang, Three-dimensional detonation structure and its response to confinement, Proc. Combust. Inst. 39 (3) (2023) 2915–2923.

[14] P. Clavin, F. A. Williams, Analytical studies of the dynamics of gaseous detonations, Philosophical Transactions of the Royal Society A: Mathematical, Physical and Engineering Sciences 370 (2012) 597–624.

[15] V. Monnier, V. Rodriguez, P. Vidal, R. Zitoun, An analysis of three-dimensional patterns of experimental detonation cells, Combust. Flame 245 (2022) 112310.

[16] V. Monnier, P. Vidal, V. Rodriguez, R. Zitoun, From graph theory and geometric probabilities to a representative width for three-dimensional detonation cells, Combust. Flame 256 (2023) 112996.

[17] V. Monnier, Aspects tridimensionnels de la détonation cellulaire : des observations expérimentales et un modèle, Ph.D. thesis, ENSMA (2023).

[18] C. M. Tarver, Chemical energy release in one-dimensional detonation waves in gaseous explosives, Combust. Flame 46 (1982) 111–133.
[19] C. M. Tarver, Chemical energy release in the cellular structure of gaseous detonation waves, Combust. Flame 46 (1982) 135–156.
[20] J. Vargas, R. Mével, M. Lino da Silva, D. A. Lacoste, Development of a steady detonation reactor with state-to-state thermochemical modeling, Shock Waves 32 (2022) 679–689.
[21] J. Vargas, K. P. Chatelain, D. A. Lacoste, X. Huang, R. Mével, Non-equilibrium effect in H_2-O_2-Diluent mixtures using the ZND reactor model, 29 th ICDERS, paper 78 (2023).
[22] I. S. Batraev, A. A. Vasil'ev, V. Y. Ul'yanitskii, A. A. Shtertser, D. K. Rybin, Investigation of gas detonation in over-rich mixtures of hydrocarbons with oxygen, Combust., Explos., Shock Waves 54 (2018) 207–215.
[23] J. Shepherd, I. Moen, S. Murray, P. Thibault, Analyses of the cellular structure of detonations, Symp. (Int.) Combust. 21 (1) (1988) 1649–1658.
[24] F. Pintgen, C. Eckett, J. Austin, J. Shepherd, Direct observations of reaction zone structure in propagating detonations, Combust. Flame 133 (3) (2003) 211–229.
[25] J. Austin, F. Pintgen, J. Shepherd, Reaction zones in highly unstable detonations, Proc. Combust. Inst. 30 (2) (2005) 1849–1857.
[26] A. Higgins, Steady one-dimensional detonations, in: F. Zhang (Ed.), Shock Waves Science and Technology Library, Vol. 6: Detonation Dynamics, Springer Berlin Heidelberg, 2012, pp. 33–105.
[27] H. D. Ng, Detonation instability, in: F. Zhang (Ed.), Shock Waves Science and Technology Library, Vol. 6: Detonation Dynamics, Springer Berlin Heidelberg, 2012, pp. 107–212.
[28] W. Fickett, W. C. Davis, Detonation, The University of California Press, Berkeley, 1979.
[29] J. Crane, X. Shi, A. V. Singh, Y. Tao, H. Wang, Isolating the effect of induction length on detonation structure: Hydrogen–oxygen detonation promoted by ozone, Combust. Flame 200 (2019) 44–52.
[30] A. Starikovskiy, N. Aleksandrov, Plasma-assisted ignition and combustion, Prog. Energy Combust. Sci. 39 (2013) 61–110.
[31] Y. Ju, W. Sun, Plasma assisted combustion: Dynamics and chemistry, Prog. Energy Combust. Sci. 48 (2015) 21–83.
[32] S. M. Starikovskaia, Plasma-assisted ignition and combustion: nanosecond discharges and development of kinetic mechanisms, J. Phys. D: Appl. Phys. 47 (2014) 353001.
[33] I. V. Adamovich, I. Choi, N. Jiang, J. H. Kim, S. Keshav, W. R. Lempert, E. Mintusov, M. Nishihara, M. Samimy, M. Uddi, Plasma assisted ignition and high-speed flow control: non-thermal and thermal effects, Plasma Sources Sci. Technol. 18 (2009) 034018.
[34] I. N. Kosarev, N. L. Aleksandrov, S. V. Kindysheva, S. M. Starikovskaia, A. Y. Starikovskii, Kinetics of ignition of saturated hydrocarbons by nonequilibrium plasma: CH_4 – containing mixtures, Combust. Flame 154 (3) (2008) 569–586.
[35] G. Ciccarelli, S. Dorofeev, Flame acceleration and transition to detonation in ducts, Prog. Energy Combust. Sci. 34 (4) (2008) 499–550.
[36] J. A. Gray, D. A. Lacoste, Enhancement of the transition to detonation of a turbulent hydrogen–air flame by nanosecond repetitively pulsed plasma discharges, Combust. Flame 199 (2019) 258–266.
[37] A. A. Tropina, R. Mahamud, Effect of plasma on the deflagration to detonation transition, Combust. Sci. Technol. (2021) 1–19.
[38] V. P. Zhukov, A. E. Rakitin, A. Y. Starikovskii, Effect of high-voltage pulsed discharges on deflagration to detonation transition, J. Propul. Power 24 (2008) 88–93.
[39] A. Tropina, R. Mahamud, D. W. Yorn, R. B. Miles, Deflagration to detonation transition assisted by equilibrium and non-equilibrium plasma, AIAA Aviation Forum (2019) 3119.
[40] Y. Zhu, V. Anand, J. Jodele, E. Knight, E. J. Gutmark, D. Burnette, Plasma-assisted rotating detonation combustor operation, in: 53rd AIAA/SAE/ASEE Joint Propulsion Conference, 2017, p. 4742.
[41] M. AliCherif, S. A. Shcherbanev, S. M. Starikovskaia, P. Vidal, Effect of non-equilibrium plasma

on decreasing the detonation cell size, Combust. Flame 217 (2020) 1–3.
[42] S. Boulal, P. Vidal, R. Zitoun, Experimental investigation of detonation quenching in non-uniform compositions, Combust. Flame 172 (2016) 222–233.
[43] S. Boulal, P. Vidal, Z. R., T. Matsumoto, A. Matsuo, Experimental investigation on detonation dynamics through a reactivity sink, Combust. Flame 196 (2018) 11–25.
[44] H. Nakayama, T. Moriya, J. Kasahara, A. Matsuo, Y. Sasamoto, I. Funaki, Stable detonation wave propagation in rectangular-cross-section curved channels, Combust. Flame 159 (2) (2012) 859–869.
[45] N. Anikin, S. Starikovskaia, A. Starikovskii, Study of oxidation of alkanes in their mixtures with oxygen and air under the action of a pulsed volume nanosecond discharge, Plasma Physics Reports 30(12) (2004) 1028.
[46] S. Gordon, B. McBride, Computer program for calculation of complex chemical equilibrium compositions and applications, i. analysis (ref. 1311), Tech. rep., NASA (1994).
[47] R. Mével, J. Sabard, J. Lei, N. Chaumeix, Fundamental combustion properties of oxygen enriched hydrogen/air mixtures relevant to safety analysis: Experimental and simulation study, Int. J. Hydrogen Energy 41 (2016) 6905–6916.
[48] I. N. Kosarev, S. O. Belov, S. V. Kindysheva, A. Y. Starikovskiy, N. L. Aleksandrov, Inhibition of plasma-assisted ignition in hydrogen–oxygen mixtures by hydrocarbons, Combust. Flame 189 (2018) 163–172.
[49] J. Delcroix, C. Ferreira, A. Ricard, Principles of Laser Plasmas ed G Bekefi, New York: Wiley, 1976.
[50] N. Popov, Effect of a pulsed high-current discharge on hydrogen-air mixtures, Plasma Phys. Report 34 (2008) 376–391.
[51] M. J. McEwan, L. F. Phillips, Chemistry of the atmosphere, New York (1975).
[52] A. I. Florescu-Mitchell, J. B. A. Mitchell, Dissociative recombination, Physics reports 430 (2006) 277–374.
[53] G. J. M. Hagelaar, L. C. Pitchford, Solving the boltzmann equation to obtain electron transport coefficients and rate coefficients for fluid models, Plasma Sources Sci. Technol. 14 (2005) 722.
[54] S. A. Lawton, A. V. Phelps, Excitation of the $b^1\Sigma_g^+$ state of O_2 by low energy electrons, J. Chem. Phys. 69 (2008) 1055–1068.
[55] C. Yamabe, S. J. Buckman, A. V. Phelps, Measurement of free-free emission from low-energy-electron collisions with ar, Phys. Rev. A: At. Mol. Opt. Phys. 27 (1983) 1345–1352.
[56] L. C. Pitchford, L. L. Alves, K. Bartschat, S. F. Biagi, M. C. Bordage, A. V. Phelps, C. M. Ferreira, G. J. M. Hagelaar, W. L. Morgan, S. Pancheshnyi, V. Puech, A. Stauffer, O. Zatsarinny, Comparisons of sets of electron–neutral scattering cross sections and swarm parameters in noble gases: I. argon, J. Phys. D: Appl. Phys. 46 (2013) 334001.
[57] S. J. Buckman, A. V. Phelps, Vibrational excitation of D_2 by low energy electrons, J. Chem. Phys. 82 (1985) 4999–5011.
[58] S. Pancheshnyi, B. Eismann, G. Hagelaar, L. Pitchford, Computer code ZDPlaskin, Laboratoire LAPLACE (UMR 5213 CNRS, INP, Univ. Toulouse III, France (2008).
[59] N. A. Popov, The effect of nonequilibrium excitation on the ignition of hydrogen-oxygen mixtures, High Temp. 45 (2007) 261–279.
[60] N. A. Popov, S. M. Starikovskaia, Relaxation of electronic excitation in nitrogen/oxygen and fuel/air mixtures: fast gas heating in plasma-assisted ignition and flame stabilization, Prog. Energy Combust. Sci. 91 (2022) 100928.
[61] D. A. Xu, M. Shneider, D. A. Lacoste, C. O. Laux, Thermal and hydrodynamic effects of nanosecond discharges in atmospheric pressure air, J. Phys. D: Appl. Phys. 47 (2014) 235202.
[62] M. Castela, S. Stepanyan, B. Fiorina, A. Coussement, O. Gicquel, N. Darabiha, C. O. Laux, A 3-D DNS and experimental study of the effect of the recirculating flow pattern inside a reactive kernel produced by nanosecond plasma discharges in a methane-air mixture, Proc. Combust. Inst. 36 (2017) 4095–4103.

[63] C. Dumitrache, A. Gallant, N. Minesi, S. Stepanyan, G. D. Stancu, C. O. Laux, Hydrodynamic regimes induced by nanosecond pulsed discharges in air: mechanism of vorticity generation, Journal of Physics D: Applied Physics 52 (36) (2019) 364001.

[64] T. J. Anderson, E. K. Dab, Measurements of normal detonation wave structure using rayleigh imaging, Symp. (Int.) Combust. 24 (1992) 1853–1860.

[65] R. A. Strehlow, R. Liaugminas, R. H. Watson, J. Eyman, Transverse wave structure in detonations, Symp. (Int.) Combust. 11 (1967) 683–692.

[66] R. A. Strehlow, Transverse waves in detonations: II. Structure and spacing in H_2-O_2, C_2H_2-O_2, C_2H_4-O_2, and CH_4-O_2 systems, AIAA J. 7 (1969) 492–496.

[67] D. Desbordes, Aspects stationnaires et transitoires de la détonation dans les gaz: relation avec la structure cellulaire du front, Ph.D. thesis, Poitiers (1990).

[68] Y. P. Raizer, Gas Discharge Physics, Vol. 2nd ed., Springer Berlin, 1991.

[69] A. Fridman, Plasma chemistry, Cambridge University Press, 2008.

[70] C. Matignon, Etude de la détonation de deux mélanges stoechiométriques ($CH_4/H_2/O_2/N_2$ et $CH_4/C_2H_6/O_2/N_2$). Influence de la proportion relative des deux combustibles et de la température initiale élevée, Ph.D. thesis, Poitiers (2000).